ARTICLE

Fluid Mud Dynamics and Its Correlation to Hydrodynamics in Jiaojiang River Estuary, China

Li Li[1,2] · Jiachen Wang[1] · Yiqun Zheng[1] · Yanming Yao[1] · Weibing Guan[1,3]

Abstract

The Jiaojiang Estuary is a macro-tidal estuary with high turbidity and funnel-shaped geomorphology. Estuarine geomorphology and shipping are highly affected by sediments and heavy coastal engineering. Based on observed data and numerical simulation results, we studied the characteristics of the suspended sediments and fluid mud in the estuary. By considering two-way coupling of water–sediment density and the process of fine sediment flocculation, a three-dimensional sediment model of the Jiaojiang Estuary was established and effectively calibrated using the measured data on tides, currents, and suspended sediment concentration (SSC). Field data analysis indicated that SSC and sediment transport rate in both the main tidal channel and shoals were positively correlated with the flow velocity in the low-frequency part during both the spring and neap tides. The model results revealed that the net sediment flux is controlled by advection and moves landward upstream of the main tidal channel. Fluid mud is formed near Haimen station, with tides influencing the spatial and temporal variations in its thickness and speed. Sediment is actively exchanged among fluid mud-water-seabed, with sink and source processes dominating near the bay mouth and the Haimen station, respectively. Sediments weaken the seaward residual currents slightly by changing their viscosity and the von Karman constant, and the stratification process is affected by changes in water density. The findings of this study provide a foundation for the study of material transportation in an estuarine ecosystem.

Keywords Tides · SSC · Fluid mud · Hydrodynamics · Jiaojiang River Estuary

1 Introduction

Estuaries connect terrestrial and oceanic environments and are subject to dynamic factors, with hydrodynamics and sediment dynamics being extremely important among them. Because of their importance with regard to biological

✉ Li Li
lilizju@zju.edu.cn

✉ Yanming Yao
hotfireyao@163.com

1 Ocean College, Zhejiang University, Zhoushan 316021, China

2 Key Laboratory of Offshore Geotechnical and Material Engineering of Zhejiang Province, Zhejiang University, Hangzhou 310058, China

3 The National Key the Laboratory of Satellite Ocean Environmental Dynamics, Ministry of Natural Resources, Hangzhou 310058, China

diversity and coastal economies, estuaries are greatly affected by human activities, such as reclamation, port development, and navigation channel construction. Water dynamics change with human activity development (Kerner 2007; Winterwerp et al. 2013), sediment transport patterns (Van Maren et al. 2015), and dynamic topography (Jeuken and Wang 2010; Monge-ganuzas et al. 2013). Therefore, studying the dynamic characteristics and transport mechanisms of estuaries is highly important.

Sediments are essential to the geomorphological evolution of estuaries. Suspended sediments coalesce in estuaries to form maximum turbidity zones and sandbars. For example, sediment flocculation near the salt-water–freshwater front induces water stratification and depresses water mixing, contributing to the formation of estuarine turbidity maximum zones and subsequent sediment deposition (e.g., the Chiangjiang River Estuary). When turbid river plumes encounter velocity shear fronts, sediments are constrained

into coastal zones to form deltas (e.g., the Yellow River Estuary).

The characteristics and mechanisms of spatiotemporal variations in suspended sediment concentration (SSC) differ across estuaries worldwide (Dyer 1986). For example, the variation in SSC in the Ashepoo Estuary is highly sensitive to the settlement of fine sediments and changes in runoff (Blake et al. 2001). In the turbid Qiantang River Estuary, the sediment dynamics are strongly affected by macro-tides and mainly controlled by periodic changes in tidal currents (Xie et al. 2018). In the Tweed Estuary, the seasonal variation in SSC is mainly influenced by fluctuations in incoming water and sediments (Uncles et al. 2000). Winds and waves are the main factors influencing sediment resuspension and transport in estuaries. Particularly in shallow water areas, the shear stress on the seabed is significantly enhanced by wave deformation, which causes the bed sediments to lift into the upper water column, correspondingly increasing the SSC (Shi et al. 2008; Zhao et al. 2019).

Sediments are correlated with water dynamics. Considering the effect of sediments on the velocity of currents, Wright (1989) suggested that the distribution of suspended sediments affects velocity by changing the bed roughness and the Carmen constant. The vertical profile of the SSC affects the flow velocity and causes water stratification by changing the vertical density. Sediment transport causes changes in the bed micro-topography (e.g., depth) and affects the flow velocity. The Carmen constant, an important parameter that reflects the influence of estuarine sediments on flow structure, is inversely proportional to the gradient variation in the flow velocity at the same gradient and water depth (Qin 1991). Several factors affect the Carmen constant, including effective suspension work and flow energy (Einstein et al. 1955; Wang 1981), SSC (Ni et al. 1988; Zhang 1995; Liu et al. 2014), and the relative viscosity coefficient (Shu et al. 2008; Zhou et al. 2008). Increased SSC leads to an increase in the relative viscosity coefficient and subsequent decrease in the Carmen constant. The inversely proportional nature of the Carmen constant to the flow velocity gradient causes variation in vertical velocity.

Suspended fine sediments at extremely high concentrations (> 10 kg/m^3) are called fluid mud (Dankers et al. 2007). Fluid mud, described as a type of high-concentration and fine-grained sediment (Mcanally et al. 2007) with a certain fluidity between the upper water column and bottom bed, represents a unique sediment phenomenon in muddy estuaries and coastal and high-turbidity estuarine areas, such as the Mississippi River Estuary (Corbett et al. 2007), Amazon River Delta (Winterwerp et al. 2006), Jiaojiang River Estuary (Guan et al. 2005), Yangtze River Estuary (Wan et al. 2014), and Lianyungang Harbor (Xie et al. 2010). Fluid mud mainly comprises water, clay, silt particles, organic matter, and pollutants, and can be

formed in an environment with sufficient fine sand supply and long-term stagnation or slow water flow. Yang (2014) summarized previous studies on the definition of fluid mud density and suggested that fluid mud density range could be reasonably defined as 1050–1200 kg/m^3. In contrast to water and suspended sediments, fluid mud has complex rheological properties ranging from elastic to quasi-plastic and can exhibit flow on an appropriately sloped plane under the action of gravity (Mcanally et al. 2007). Fluid mud has an attenuation effect on free surface water and shallow waves (Xia et al. 2011, 2014). Wave energy is dissipated because of the shear motions and viscosity within the upper mud layer, and the elastic absorption of the lower mud layer dissipates the wave energy. The thickness and viscosity of fluid mud can influence the stability of the fluid mud-water interface, with both playing an important role in the evolution of the fluid mud-water interface (Liu et al. 2021). In estuaries and tidal flats, sediment transport processes, such as flocculation, deposition, and entrainment occur simultaneously, with a close relationship existing between the entrainment rate and the density distribution of fluid mud in the vertical direction (Xu et al. 2020).

The Jiaojiang River Estuary (Fig. 1a) is located on the middle coast of the East China Sea. The bay has an energetic hydrodynamic process owing to the effect of the Jiaojiang River runoff (average annual runoff is approximately 51.72×10^8 m^3) and macro-tides (mean tidal range of 2.9–4.2 m) (Jiang 2017). The bay is highly turbid with strong tides and sufficient fine sediments. Various studies have been conducted on the factors affecting the suspended sediments in the Jiaojiang Estuary, such as salt-freshwater mixing (Zhao 1992), water stratification and mixing (Geyer 1993; Dong 1998), lutocline (Jiang et al. 1998), and waves (Wang 2007). Field data have demonstrated that sediment scouring and silting are closely related to the Jiaojiang River runoff, and the products of scouring and silting are mainly flocculated suspended sediments (Bi et al. 1984; Fu et al. 1989). Li and Wolanski (1993) focused on the flocculation of suspended sediments in the Jiaojiang Estuary and suggested the presence of unbreakable 'dense flocs' and fragile 'loose flocs'. Large and dense flocs facilitate the formation of fluid mud (Tran and Storm 2019). Flocs are several orders of magnitude larger than fine sediments and tend to settle faster (He et al. 2017).

The Jiaojiang Estuary, being a muddy estuary, contains fluid mud. Dong et al. (1997) studied the variations in sediment source and concentration in the estuary and found that the sediment transported into the estuary by tidal currents was considerably greater than that transported by runoff. Fluid mud was found near the bottom of the Jiaojiang Estuary, which reduced the resistance coefficient of the seabed. Based on a three-dimensional numerical model, Guan et al. (2005) studied the distribution and variation of
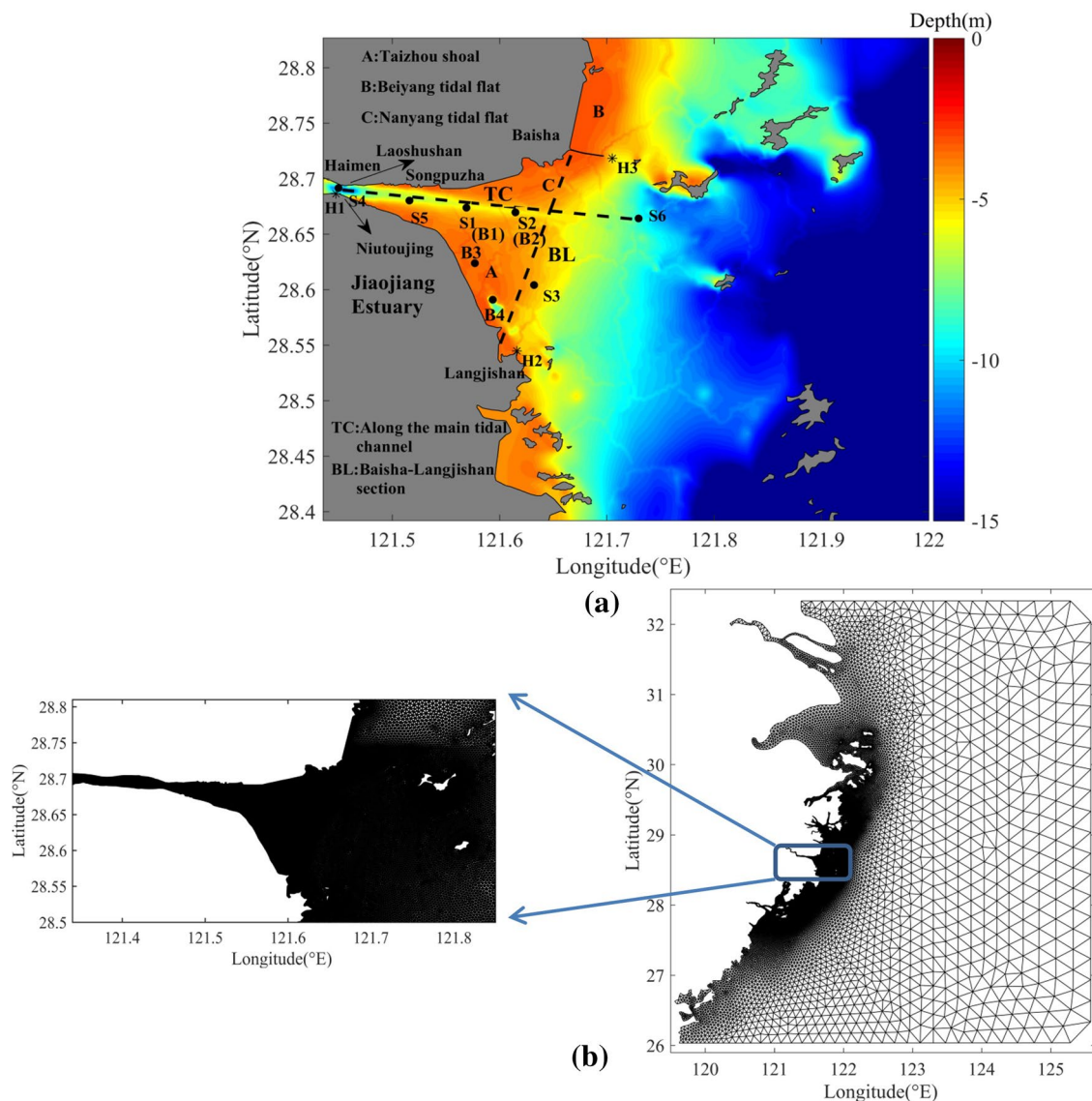
Fig. 1 **a** The distribution of field stations in the Jiaojiang Estuary (1985 national height datum). **b** The model grids of the Jiaojiang Estuary

fluid mud in the horizontal and longitudinal sections of the Jiaojiang Estuary and confirmed the formation of fluid mud near the bottom level. Based on field data, Xie et al. (1998) found a 1 m thick fluid mud layer in the Jiaojiang Estuary.

In this study, we examined the temporal and spatial characteristics of suspended sediments and fluid mud using field data and a well-calibrated numerical model. The physical mechanisms of suspended sediments and fluid mud, as well as the impact of sediments on currents and stratification, are discussed. Section 2 describes the methodology, including the field data and numerical model. Section 3 presents the results, and we discuss the results in Sect. 4. Conclusions are summarized in Sect. 5.

2 Methodology

2.1 Field Data

The distribution of field stations in the Jiaojiang Estuary is shown in Fig. 1a. With five stations arranged along the axis of the main tidal channel and one in the Taizhou shoal. Data on tidal levels, vertical profile of tidal currents, salinity, and SSC were collected at the six stations. Observations from three stations, H1-H3 (Haimen, Langjishan, and Baishashan), were used to obtain long-term tidal data from Aug 16 to Sept 9, 2014 (Table 1). Field data from July 1 to July 10, 2013 were also obtained using the same method (Table 1).

Table 1 Time periods and methods of data collection

Stations	Time periods	Parameters
H1-H3	August 16–September 9, 2014 July 1–July 10, 2013	Tidal level[a]
S1-S6 B1-B4	Spring tide and neap tide[c]	Current speeds and directions, SSC, Salinity[b]

[a]Current speeds and directions of six uniform layers were measured (surface, − 0.2H, − 0.4H, − 0.6H, − 0.8H, bottom, where H represents the mean water depth)

[b]The salinity and SSC were obtained by water sample analysis (surface, − 0.6H, bottom)

[c]Sampling periods include spring tides (August 26, 08:00 to August 27, 11:00, 2014; July 9, 15:00 to July 10, 18:00, 2013) and neap tides (September 3, 08:00 to September 4, 11:00, 2014; July 2, 10:00 to July 3, 12:00, 2013)

Tidal level data were recorded using a self-recording tidal gage (TGR-2050) at 1 h intervals. The current data were measured in six uniform layers using current meters (SLC9-2) every 10 min. SSC and salinity data were obtained by analyzing water samples collected using a horizontal sampler (XCL-2L) in the laboratory. Bottom mud samples were obtained using a mussel sampler (Dawn HNM-2). A DGPS positioning system (DGPS-MAX) was used for geographical positioning during the observation periods. The suspended sediment samples were oven-dried and salt-washed. SSC was then defined according to the ratio of dry sediment weight to water sample volume (kg/m^3).

2.2 Numerical Model

2.2.1 Model Descriptions

The finite volume coastal ocean model (FVCOM) is a three-dimensional ocean dynamic numerical model (Chen et al. 2003). The momentum and continuity equation of the FVCOM hydrodynamic module in the Cartesian coordinate system are expressed as follows:

$$\frac{\partial u}{\partial t} + u\frac{\partial u}{\partial x} + v\frac{\partial u}{\partial y} + w\frac{\partial u}{\partial z} - fv = -\frac{1}{\rho}\frac{\partial P}{\partial x} + \frac{\partial}{\partial z}(K_m\frac{\partial u}{\partial z}) + F_u \tag{1}$$

$$\frac{\partial v}{\partial t} + u\frac{\partial v}{\partial x} + v\frac{\partial v}{\partial y} + w\frac{\partial v}{\partial z} + fu = -\frac{1}{\rho}\frac{\partial P}{\partial y} + \frac{\partial}{\partial z}(K_m\frac{\partial v}{\partial z}) + F_v \tag{2}$$

$$\frac{\partial w}{\partial t} + u\frac{\partial w}{\partial x} + v\frac{\partial w}{\partial y} + w\frac{\partial w}{\partial z} = -\frac{1}{\rho}\frac{\partial P}{\partial z} + \frac{\partial}{\partial z}(K_m\frac{\partial w}{\partial z}) + F_w \tag{3}$$

$$\frac{\partial P}{\partial z} = -\rho g \tag{4}$$

$$\frac{\partial u}{\partial x} + \frac{\partial v}{\partial y} + \frac{\partial w}{\partial z} = 0 \tag{5}$$

where x, y, and z are the east, north, and vertical coordinates, respectively, and u, v, and w are the corresponding velocity components. P is atmospheric pressure, f is the Coriolis force parameter, ρ is the density of seawater, and g is the acceleration of gravity. F_u, F_v, and F_w are momentum diffusion terms in x, y, and z directions. K_m is the vertical eddy viscosity coefficient. The Smagorinsky turbulence closure (Smagorinsky 1963) and Mellor-Yamada level 2.5 (Mellor et al. 1982) schemes were adopted in the model for horizontal and vertical calculation, respectively.

The σ-coordinate transformation is defined as follows:

$$\sigma = \frac{z-\zeta}{H+\zeta} = \frac{z-\zeta}{h} \tag{6}$$

where H is the depth from the bottom to the mean sea level, ζ is the height from the free surface to the average sea level, and h is the actual water height. σ varies from 0 at the surface to − 1 at the bottom.

The diffusion equations of SSC in the model are as follows:

$$\frac{\partial C}{\partial t} + \frac{\partial uC}{\partial x} + \frac{\partial vC}{\partial y} + \frac{\partial(w-w_s)C}{\partial z} = \frac{\partial}{\partial x}(A_H\frac{\partial C}{\partial x}) + \frac{\partial}{\partial y}(A_H\frac{\partial C}{\partial y}) + \frac{\partial}{\partial z}\left[(K_H + K_{HB})\frac{\partial C}{\partial z}\right] \tag{7}$$

where x, y, and z are defined as above; C is the suspended sediment concentration; w_s is the settling velocity of suspended sediments (positive downward); A_H is the horizontal eddy viscosity coefficient; K_H is the vertical eddy viscosity coefficient; and K_{HB} is the background value of the vertical eddy viscosity coefficient.

The sedimentation velocity formula proposed by Cao is used to calculate the sedimentation velocity (Cao et al. 2010; Xu et al. 2018):

$$\omega_s = \omega_{s0}K_f\frac{1+c_2C^{m_2}}{1+c_1U^{m_1}} \tag{8}$$

$$K_f = C_fC_D = \left(0.00177D_{50}^{-1.82}\right)C_D \tag{9}$$

$$C_D = \left[1 + 0.12\lg\left(\frac{0.03}{D_{50}}\right)\right]e^{(1.1\times10^5D_{50}^2-99)S_t} \tag{10}$$

where w_{s0} is the settling velocity of single particle sediment, U is the flow velocity, K_f is the mixing coefficient of salt-fresh water, and S_t is the salinity. When the median particle size of the sediments (D_{50}) is greater than 0.0307 mm, K_f is 1.0. c_1, c_2, m_1, m_2 are the empirical parameters obtained through model debugging.

The equations of the planar two-dimensional fluid mud model are as follows:

$$\frac{\partial d_m}{\partial t} + \frac{\partial u_m d_m}{\partial x} + \frac{\partial v_m d_m}{\partial y} = \frac{1}{c_m}\frac{dM}{dt} \tag{11}$$

$$\frac{\partial u_m d_m}{\partial t} + u_m\frac{\partial u_m d_m}{\partial x} + v_m\frac{\partial u_m d_m}{\partial y} - fv_m d_m = \\ -gd_m\frac{\rho_m - \rho}{\rho_m}\frac{\partial \eta_m}{\partial x} - \frac{1}{\rho_m}\left(\tau_{m,bx} - \tau_{m,sx}\right) - \frac{d_m}{\rho_m}\rho g\frac{\partial \eta}{\partial x} \tag{12}$$

$$\frac{\partial v_m d_m}{\partial t} + u_m\frac{\partial v_m d_m}{\partial x} + v_m\frac{\partial v_m d_m}{\partial y} + fu_m d_m = \\ -gd_m\frac{\rho_m - \rho}{\rho_m}\frac{\partial \eta_m}{\partial y} - \frac{1}{\rho_m}\left(\tau_{m,by} - \tau_{m,sy}\right) - \frac{d_m}{\rho_m}\rho g\frac{\partial \eta}{\partial y} \tag{13}$$

where d_m is fluid mud thickness, u_m and v_m are the flow velocities of fluid mud in x and y directions. $\frac{1}{c_m}\frac{dM}{dt}$ is the source term of fluid mud mass change, c_m is the mean sediment concentration of fluid mud. $\frac{dM}{dt}$ is the mass exchange flux between fluid mud and upper water and lower bed surface. ρ_m is the average density of floating mud. ρ is the upper water density. $\eta_m = Z + d_m$ is the surface elevation of fluid mud (bottom bed elevation + fluid mud thickness). η is the free surface elevation of the upper water column. $\tau_{m,bx}$ and $\tau_{m,by}$ are the components of the shear stress in the x and y directions between the fluid mud and the bed surface. $\tau_{m,sx}$ and $\tau_{m,sy}$ are the components of the shear stress between the fluid mud and the upper water in the x and y directions.

The formation and decomposition of fluid mud are mainly determined by the source-sink term in Eq. 14, including the settling flux (Settling), resuspension flux (Entrainment), erosion flux (Erosion), and consolidation of suspended sediments in the upper water (Dewatering), calculated as follows:

$$\frac{dM}{dt} = Settling - Entrainment + Erosion - Dewatering \tag{14}$$

The calculation formula is as follows:

$$Settling = H(\frac{\tau_{dm} - \tau_{m,s}}{\tau_{dm}})w_s C_b(\frac{\tau_{dm} - \tau_{m,s}}{\tau_{dm}}) \tag{15}$$

$$Entrainment = \frac{2C_s\left[|u_{*,m}|^2 - \tau_B/\rho\right]\Delta u + C_\sigma\left[|u_{*,s}|^2 - \tau_B/\rho\right]|u_{*,s}|}{\frac{gh\Delta\rho}{\rho_m} + C_s\Delta u^2}c_m \tag{16}$$

$$Erosion = H(\frac{\tau_{e,b} - \tau_e}{\tau_e})M_e(\frac{\tau_{e,b} - \tau_e}{\tau_e}) \tag{17}$$

$$Dewatering = V_0 c_m \tag{18}$$

where H is the Heaviside step function. τ_{dm} is the critical shear stress of the sedimentation flux, and C_b is the SSC of the water above the fluid mud. $u_{*,s}^3 = u_*^3 + u_{*,m}^3$, u_* is the friction velocity of the upper water column, $u_{*,m}^2 = f_s\Delta u^2$. The empirical coefficients C_s and C_σ are 0.25 and 0.42, respectively. M_e is the bed erosion coefficient, τ_e is the erosion critical shear stress, $\tau_{e,b}$ is the shear stress between fluid mud and bottom bed. V_0 is consolidation rate of fluid mud. M_e and V_0 are 0.0005 and 0.00001, respectively (Yang 2014).

Wang et al. (1998) verified the drag reduction of fluid mud by flume experiments, and proposed the friction coefficient formula:

$$f = 8 \times \frac{u^*}{U^2} \tag{19}$$

$$f_s = R \times f = \frac{1}{1 + AR_f} \times 8\frac{u_*^2}{U^2} \tag{20}$$

where U is the average velocity of water above the fluid mud layer, u^* is the velocity of fluid mud layer. $A = 5.5$. R is the drag reduction coefficient, R_f is flux Richardson number, which can be calculated by the following formula (Mellor et al. 1974):

$$R_f = 0.725\left[R_i + 0.186 - \sqrt{R_i^2 - 0.316R_i + 0.0346}\right] \tag{21}$$

where R_i can be calculated by formula 27.

The friction coefficient between the fluid mud and the sea bed is calculated according to Yang et al. (2015):

$$f_m = \frac{24}{Re_B\left(1 - \frac{3N_e}{2} + \frac{N_e^3}{2}\right)} \tag{22}$$

$$Re_B = \frac{\rho_m U_m h}{\mu}, \quad N_e = \frac{\tau_B}{\tau_0}, \tag{23}$$

where Re_b is Bingham Reynolds number. τ_0 is the bottom shear stress. τ_B is yield stress. μ is the viscosity coefficient of the Bingham body.

According to Formulas 19 to 23, the f_s can be determined as 0.001–0.01, and the f_m can be determined as 0.015–0.1 (Yang 2014).

In estuary, pressure has little effect on density, which is mainly determined by salinity and temperature. Without considering the pressure, the formula for estimating sea-water density given by Geyer and Maccready (2014) can be used:

$$\rho = \rho_w \left(1 + \beta S_w\right) \tag{24}$$

where β is the constant value (Burchard et al. 2011), $\beta = 7.8 \times 10^{-4}$ psu^{-1}, S_w is the salinity, $S_w = 35$ psu. ρ_w is the sea-water density, which can be calculated by Bigg's (2002) formula:

$$\rho_w = a_0 + a_1 t + a_2 t^2 + a_3 t^3 + a_4 t^4 + a_5 t^5 \tag{25}$$

where $a_0 = 999.842594$, $a_1 = 6.793952 \times 10^{-2}$, $a_2 = -9.095290 \times 10^{-3}$, $a_3 = 1.001685 \times 10^{-4}$, $a_4 = -1.120083 \times 10^{-6}$, $a_5 = 6.536332 \times 10^{-9}$. $T = 28$ ℃.

The density can be estimated by volumetric relation when SSC is high (Wang 2002):

$$\rho_{ss} = \rho + \left(1 - \frac{\rho}{\rho_s}\right) C \tag{26}$$

where ρ is clear sea-water density, ρ_s is sediment density, $\rho_s = 2650$ kg/m^3, C is SSC (kg/m^3).

We use the Richardson number (Holzman 1943) and potential energy anomaly φ (Pu et al. 2015) to show the stratification:

$$Ri = -\frac{g}{\rho} \frac{\partial \rho}{\partial z} \left(\frac{\partial u}{\partial z}\right)^{-2} \tag{27}$$

$$\phi = \frac{1}{h} \int_{-h}^{0} (\overline{\rho} - \rho) gz \, dz \tag{28}$$

$$\overline{\rho} = \frac{1}{h} \int_{-h}^{0} \rho \, dz \tag{29}$$

where $\rho = \rho_{ss}$, $\overline{\rho} = \overline{\rho_{ss}}$ is vertical mean density. $Ri > 0.25$ indicates stratification, $Ri < 0.25$ indicates mixing. The larger the φ value is, the stronger the stratification is.

2.2.2 Model Configurations

We used unstructured grids suitable for simulating estuarine and coastal tidal currents in our model, with the model domain covering the entire Jiaojiang River Estuary (Fig. 1b). The estuary geometry and water depth are displayed in Fig. 1b.

The model grid comprised 70,694 elements and 37,416 nodes on the horizontal plane, after incorporating coastline data from the GSHHS database and water depth data from the ETOPO1 Global Relief Model. The cell sizes ranged from 150 m near the edge of the shoal and islands to 35,000 m at the open boundary. To accurately simulate the vertical variation in currents, we specified six uniform vertical layers in the water column using the σ-coordinate system.

The open-boundary conditions for water level were specified using the TPXO7.2 Global Ocean Tidal Model (http://volkov.oce.orst.edu/tides/TPXO7.2.html), which considered 13 hourly tidal elevations (M$_2$, S$_2$, N$_2$, K$_2$, K$_1$, O$_1$, P$_1$, Q$_1$, M$_f$, M$_m$, M$_4$, MS$_4$, MN$_4$).

Increase in sediment concentration above a certain limit creates conditions conducive for fluid mud formation. Combined with the actual situation in the Jiaojiang Estuary, the critical sediment concentration for fluid mud formation was set at approximately 10 kg/m^3. The friction coefficient f_m between the fluid mud and the bottom bed, friction coefficient f_s between the fluid mud and upper water column, bed erosion coefficient M_e, and fluid mud

Table 2 Parameter setting of the numerical model

Parameters	Values
Domain	120.056–125.480°E; 6.375–32.226°N
Elements and nodes	70,694, 37,416
Model time step	1.0 s
Vertical layers	6 layers
Runoff	Yangtze River, Qiantang River, Jiaojiang River
D_{50} (mm)	0.007
Porosity	0.5
K_f, $c1$, $c2$, $m1$, $m2$	1.0, 0.06, 4.60, 0.75, 0.60
Critical starting stress (N/m^2)	0.1–0.3
Sediment erosion rate (kg/m^2/s)	0.00005–0.00066
Bottom roughness (m)	0.00007–0.002
Bed erosion coefficient	0.0005
C_s and C_σ	0.25, 0.42
Friction coefficients f_m, f_s	0.08, 0.003
Consolidation rate V_0	0.00001

consolidation rate V_0 in the model were set as 0.08, 0.003, 0.0005, and 0.00001, respectively (Table 2).

2.2.3 Model Validations

The correlation coefficient (*CC*) and model evaluation coefficient (*SS*) were used to evaluate the model accuracy, as follows:

$$CC = \frac{1}{N} \sum_{i=1}^{N} \frac{(m_i - \overline{m})(O_i - \overline{O})}{S_m S_o} \qquad (30)$$

$$SS = 1 - \frac{\sum_{i=1}^{N}(m_i - O_i)^2}{\sum_{i=1}^{N}(O_i - \overline{O})^2} \qquad (31)$$

where O_i and m_i are the measured and calculated values, respectively, $\overline{O}, \overline{m}$ are the average values of the observations and simulations. S_O and S_m are the standard deviations of the observations and simulations respectively. The closer *CC* is to 1, the greater the correlation between the calculated and observed values. Although any *SS* value greater than 0.2 grants a certain credibility to the numerical model, a value greater than 0.5 implies high credibility (Allen et al. 2007).

The tide levels were verified against measured tide levels at three tide stations (H1-H3: Haimen, Langjishan, and Baishashan) from August 16 to September 16, 2014 and July 1 to July 10, 2013 (H1, H2 and, H3 in Fig. 1a). The simulated values agreed satisfactorily with the measured values (Fig. 2). Error analysis of the three tidal stations is presented in Table 3.

The current speeds and directions were verified using the vertical profile of current data measured at the six stations (S1, S2 (T2), S3, S4, S5, and S6 in Fig. 1a) in the Jiaojiang Estuary during the spring tides from 8: 00 on August 26,

Table 3 Error analysis of tidal stations

Stations	*CC*	*SS*
H1(2014)	0.9814	0.9232
H2	0.9930	0.9319
H3	0.9942	0.9465
H1(2013)	0.9807	0.9188
H2	0.9970	0.9424
H3	0.9975	0.9574

2014 to 11: 00 on the next day, and the neap tides from 8: 00 on September 3, 2014 to 11: 00 on the next day. Satisfactory layer-wise verification results of the currents were obtained at stations S1, S2 (T2), S3, S4, S5, and S6, and the mean errors of the corresponding stations are presented in Table 4. The results indicate that the hydrodynamic model is highly reliable and accurate.

The model was also applied for the month of July 2013 and the results were validated using field data at stations B1, B2, B3, and B4 (Fig. 3), which confirmed that the model satisfactorily reproduced the hydrodynamics in the bay (Zheng 2021).

The validation SSC for 2013 is illustrated in Fig. 4. The model reproduced the magnitudes and trends, as well as the temporal and spatial variations in SSC in the bay. In 2014, the maximum SSC of station S6 was 4.0 kg/m^3, whereas that in the observation data of Liu et al. (2018) was 18 kg/m^3. The reason for the difference may be that the sampling depth in 2014 was 1 m above the seabed, and the high-turbidity fluid mud layer near the seabed was not involved.

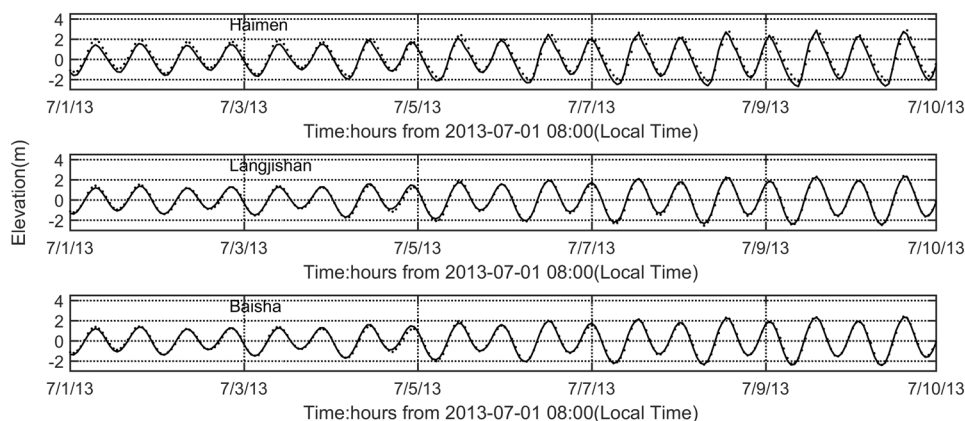**Fig. 2** Verification of tidal level at the three stations

Table 4 Error analysis of vertical-averaged velocity and direction

Stations	Spring tide				Neap tide			
	CC	SS	CC	SS	CC	SS	CC	SS
	Velocity		Direction		Velocity		Direction	
S1	0.96	0.83	0.84	0.63	0.97	0.91	0.87	0.72
S2 (T2)	0.95	0.85	0.89	0.75	0.95	0.82	0.94	0.88
S3	0.98	0.95	0.92	0.83	0.97	0.86	0.88	0.71
S4	0.91	0.80	0.96	0.84	0.96	0.84	0.86	0.68
S5	0.96	0.90	0.91	0.72	0.93	0.85	0.82	0.52
S6	0.98	0.95	0.80	0.60	0.94	0.86	0.81	0.55
B1	0.97	0.91	0.84	0.64	0.97	0.89	0.79	0.54
B2	0.98	0.93	0.75	0.44	0.96	0.83	0.90	0.79
B3	0.95	0.81	0.89	0.78	0.93	0.85	0.85	0.66
B4	0.87	0.74	0.90	0.78	0.91	0.77	0.91	0.82

3 Results

3.1 Correlation of Flow, SSC and Sediment Transport Rate

To discuss the relationship among flow velocity, SSC, and instantaneous sediment transport rate, the wavelet analysis was carried out. The original signal $S = a1 + d1$, $a1$ can be decomposed into $a2 + d2$, and $a2$ can be decomposed into $a3 + d3$, so $S = a3 + d3 + d2 + d1$. $a3$ represents the long-term trend, indicating the low-frequency change process of the signal. di ($i = 1, 2, 3$) represents the high-frequency change process. The decomposition results were normalized:

$$x_{i0} = \frac{x_i - x_{\min}}{x_{\max} - x_{\min}} \tag{27}$$

where x_{i0} is the result of normalization at the i-th moment, $x_{\min}$ and $x_{\max}$ are the minimum and maximum values in the time series, respectively.

To study the dynamic mechanism of suspended sediment transport in the Jiaojiang Estuary, the hourly vertical-averaged velocity, vertical-averaged SSC, and instantaneous sediment transport rate calculated at stations S1, S3, and S4 were analyzed based on field data. These three stations were selected because they covered the narrow and wide parts of the main tidal channel as well as the shoal of the bay. The normalized analysis results, presented in Fig. 5a–c, indicate that the SSC and sediment transport rates of the three stations are closely related to the flow velocity in the low-frequency part $a3$. Although the SSC and instantaneous sediment transport rate at S1, which is located in the main tidal channel, exhibit similar changes to flow velocity, they generally lag behind the changes in flow velocity; in contrast, the changes in the same values at S3 and S4, located in the Taizhou shoal, generally precede those of flow velocity.

In the high-frequency $d2$ part, the changes in the sediment transport and flow rates were always synchronized at S1, and the change in SSC lagged behind those in flow and sediment transport rates only in the first tidal cycle. In the $d1$ part, the high-frequency vibration waveforms of SSC and sediment transport rate at S1 are highly similar, and SSC has a noticeable effect on the change in sediment transport rate.

3.2 Hydro and Suspended Sediment Characteristics

3.2.1 Tides

The Jiaojiang estuary has semi-diurnal and macro-tidal tides, with maximum tidal ranges of 6.02, 5.86 and 5.83 m at station H1, H2, and H3 respectively. The amplitude of the M_2 tide peaks at 1.82 m in the main tidal channel. The average flooding tidal duration is approximately 1.5 h shorter than the ebbing tides.

The current distributions during spring tides are presented in Fig. 6. The direction of flood current is northwest, whereas that of the ebb current is the opposite. The tidal flow has a clockwise rotation, with the magnitude gradually decreasing from east to west. After tidal currents propagate into the estuary, the flow reciprocates owing to the restriction in topography. Owing to friction at the bottom, the corresponding velocity is generally approximately 32.4% lower than that at the surface. The duration of ebb currents is longer than that of flood currents because of the combined effects of runoff and topography.

Semi-diurnal tidal currents are dominant in the studied estuary, and the motion form of tidal currents can be characterized by the ellipticity K of the M_2 tide ($K = W_{\min}/W_{\max}$, $W_{\min}$ is the minimum current speed value, while $W_{\max}$ is the maximum current speed value). When the K is larger/smaller than 0.25, the flow is rotational/reciprocate. Positive or negative K values indicate the
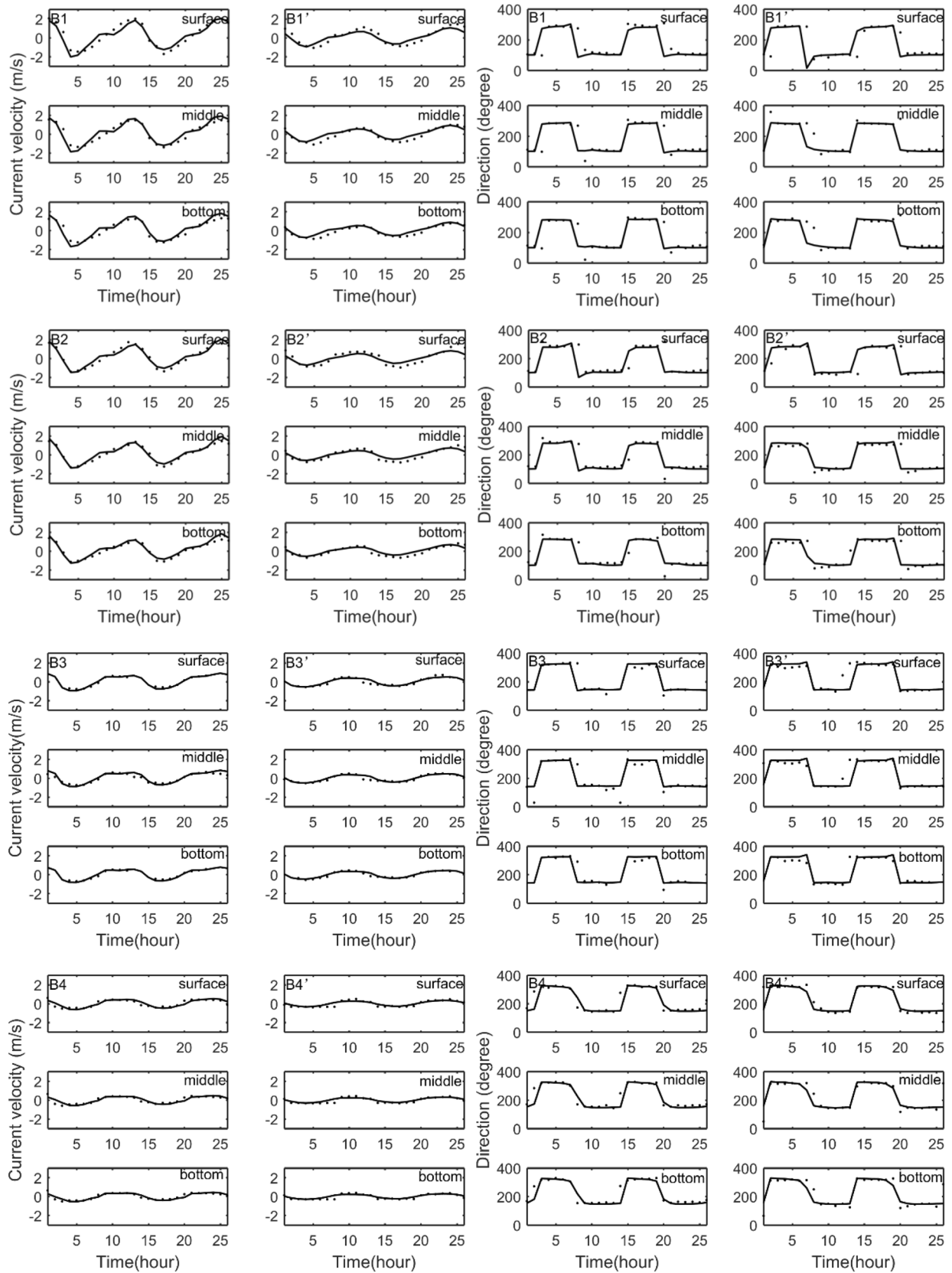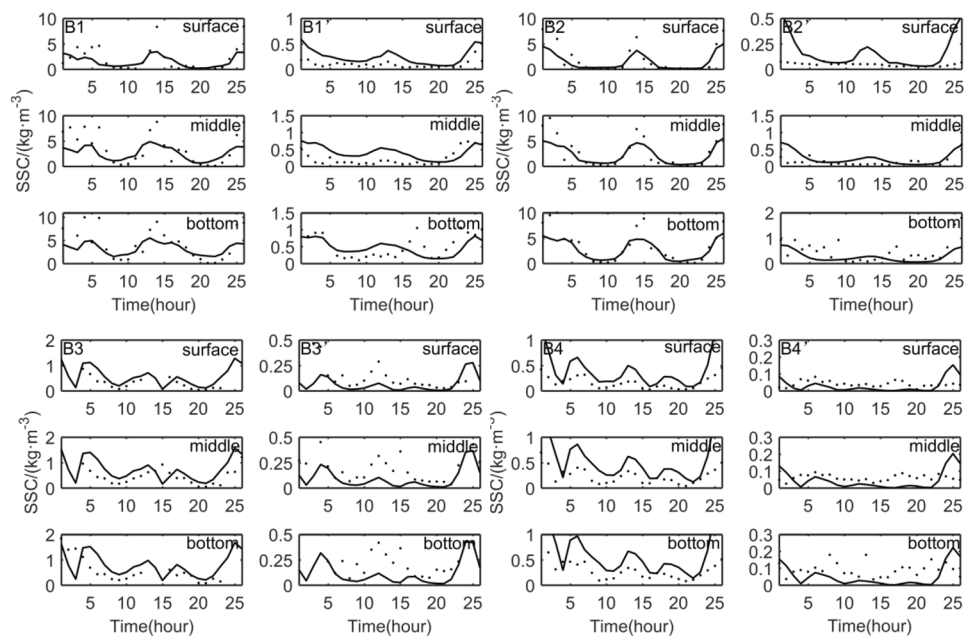
Fig. 3 Verification of velocity and direction (**B1**–**B4** are for spring tides, **B1'**–**B4'** are for neap tides)

Fig. 4 Verification of SSC (**B1**–**B4** are for spring tides, **B1'**–**B4'** are for neap tides)

counterclockwise or clockwise direction of the flow. Based on the harmonic analysis of tidal currents from August 15 to September 15, 2014, the surface and bottom tidal ellipses of M_2 tide were obtained (Fig. 6). The results of elliptic major-axis f_{max}, minor-axis f_{min}, inclination angle $finc$, and ellipticity K of vertical-average currents at the seven stations (S1, S2 (T2), S3, S4, S5, and S6) are presented in Table 5.

The results reveal a rotating flow in the open sea (Fig. 6). In the near-shore waters of the estuary, the tidal current ellipses are almost a straight line, indicating reciprocating flow. The maximum velocity of the reciprocating flow is higher than that of the rotational flow. In the coastal area, especially the main tidal channel of the estuary, the directions of the major axes of the tidal ellipses are parallel to the shoreline. Moreover, the elliptical major and minor axes gradually decrease from the surface to the bottom of the estuary owing to bottom friction.

According to the harmonic analysis results (Fig. 6 and Table 5), the absolute values of ellipticity K at all six stations were less than 0.25. Compared with the tidal constituents M2, the maximum velocity of S2 is only approximately one-third that of M2, which is the highest at station S4 (59 cm/s).

3.2.2 SSC

Figure 7 illustrates the SSC values of the Jiaojiang Estuary during the spring tidal period. The high-SSC area is mainly located on the west side of section BL. During the

flood tidal period, SSC gradually increases from the bay mouth to head along the main tidal channel.

Temporally, the main tidal channel exhibited higher SSC during spring tides than during ebb tides owing to stronger currents during spring tides. During the peak flood of the spring tides, sediments were mainly distributed near Niutoujing (Laoshushan-Songpuzha). The maximum SSC at the surface and bottom level reached 5 kg/m^3 and greater than 10 kg/m^3, respectively, followed by the SSC near Zhaipu. The SSC value near the northern bank was lower than that near the southern bank west of section BL during high slack water. The SSC value at the surface (8 kg/m^3) was lower than that at the bottom (10 kg/m^3). The SSC distribution during the neap tide was similar to that during the spring tide, but with smaller magnitude. The SSC in the main tidal channel during the neap tide was very low, owing to weak currents.

4 Discussions

4.1 Fluid Mud

The SSC was significantly higher at the bottom (> 10 kg/m^3) than at the surface, and the maximum SSC was distributed in the waters near Niutoujing and Zhaipu-Haimen at the bottom, providing conducive conditions for the formation of fluid mud. The horizontal distribution of the siltation thickness of fluid mud at the maximum and minimum range moments during July 2–3 and July 9–10, 2013 are presented in Fig. 8. The distribution range and thickness of the fluid mud were higher during the neap tidal period
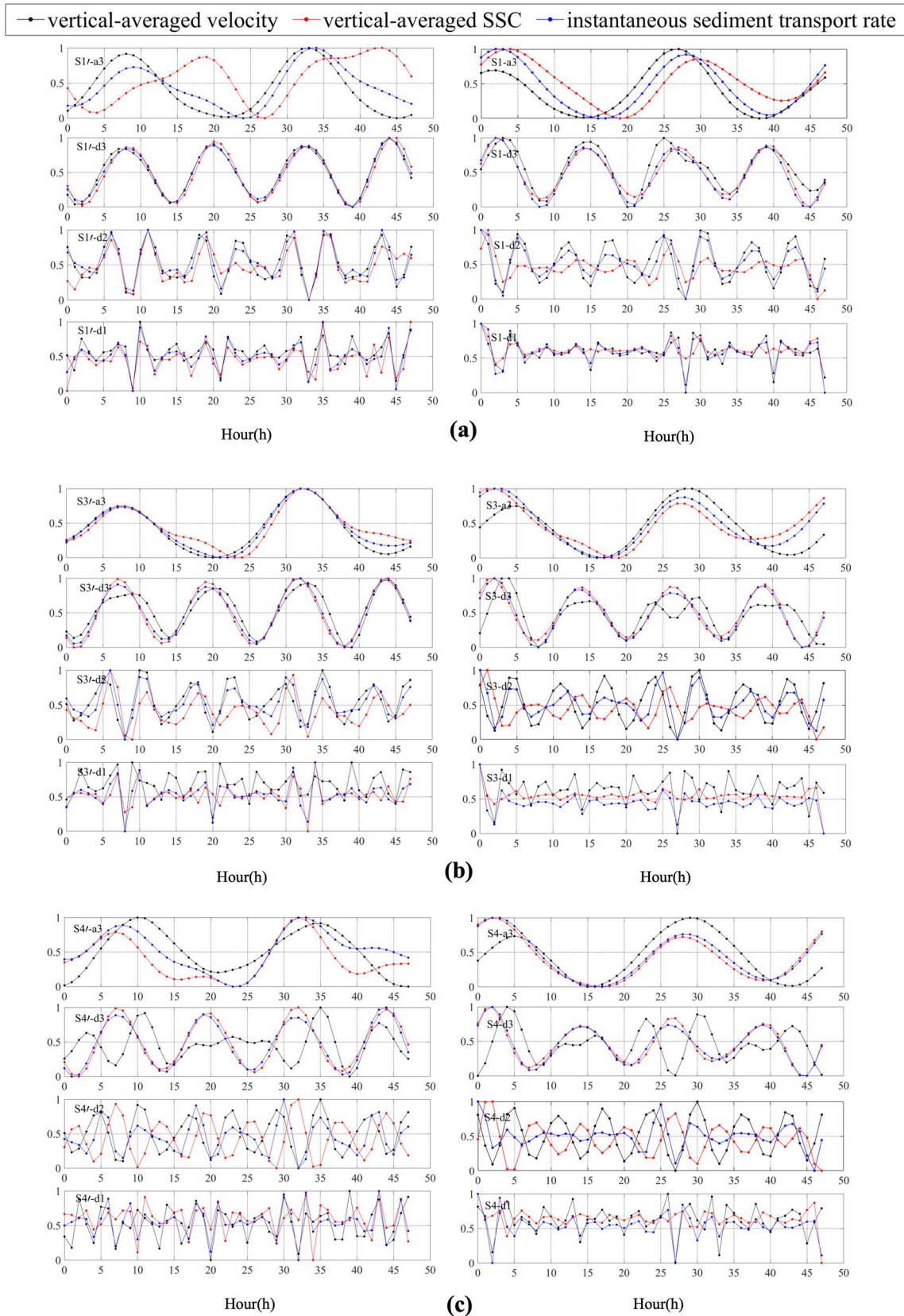
Fig. 5 Wavelet analysis of **a** S1, **b** S2, **c** S3 (left: spring tide, right: neap tide)
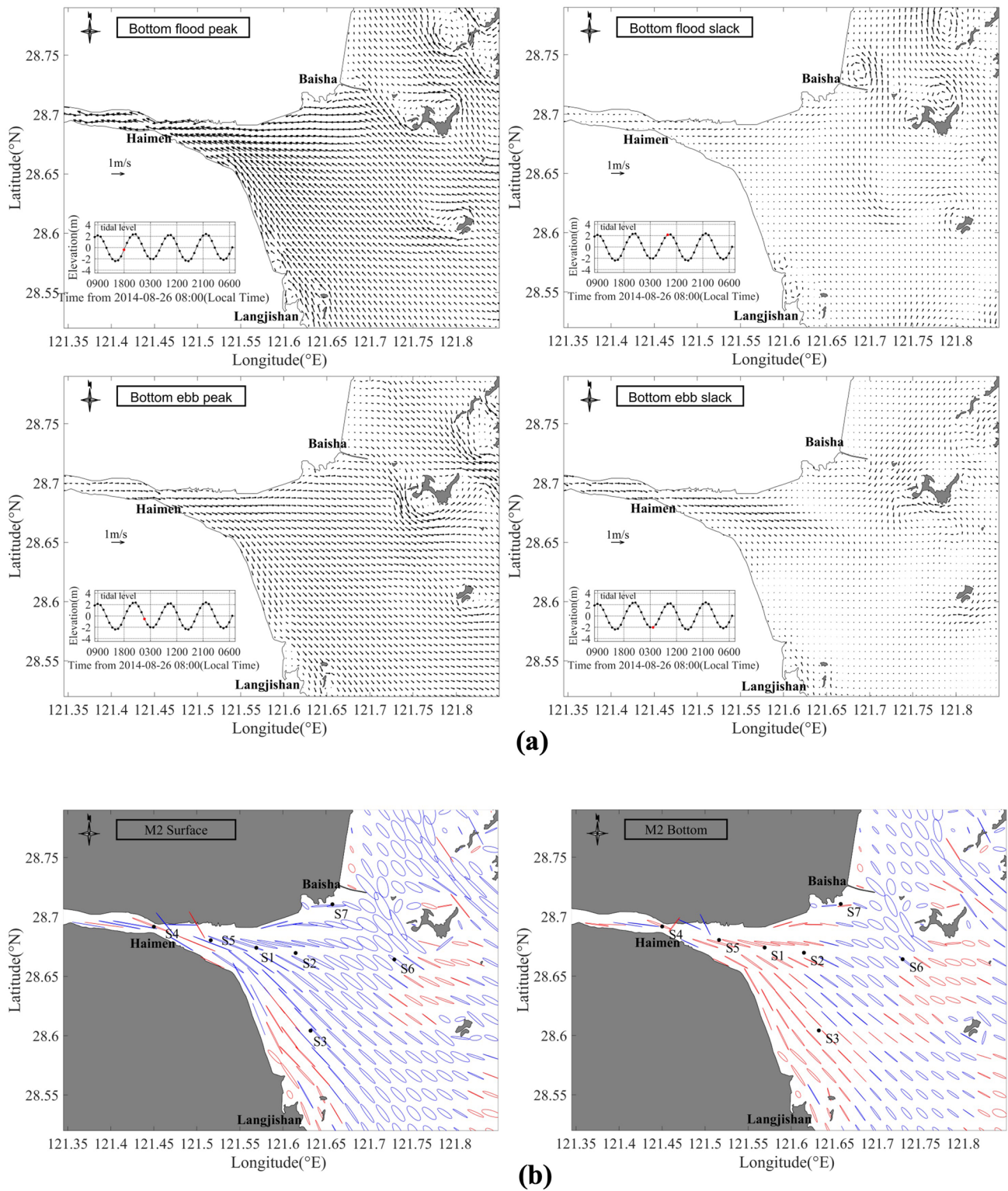
(a)

(b)

Fig. 6 **a** Bottom currents distribution during the spring tide. **b** Current ellipses distribution of M2 in surface (left) and bottom (right). Blue represents clockwise, while red represents counterclockwise

Table 5 Parameters of current ellipses at the feature points

Feature points	M₂				S₂			
	$Fmax$ (cm/s)	$Fmin$ (cm/s)	K	$Finc$ (°)	$Fmax$ (cm/s)	$Fmin$ (cm/s)	K	$Finc$ (°)
S1	116.8	0.6	0.01	110	46.7	0.2	0.01	110
S2 (T2)	93.3	0.9	− 0.01	107	37.3	0.4	− 0.01	107
S3	61.7	2.8	− 0.04	307	24.7	1.1	− 0.04	126
S4	147.4	3.8	0.03	105	59	1.5	0.03	105
S5	118.3	5.3	0.05	286	47.3	2.1	0.05	106
S6	51.8	9.7	− 0.19	287	20.7	3.9	− 0.19	117
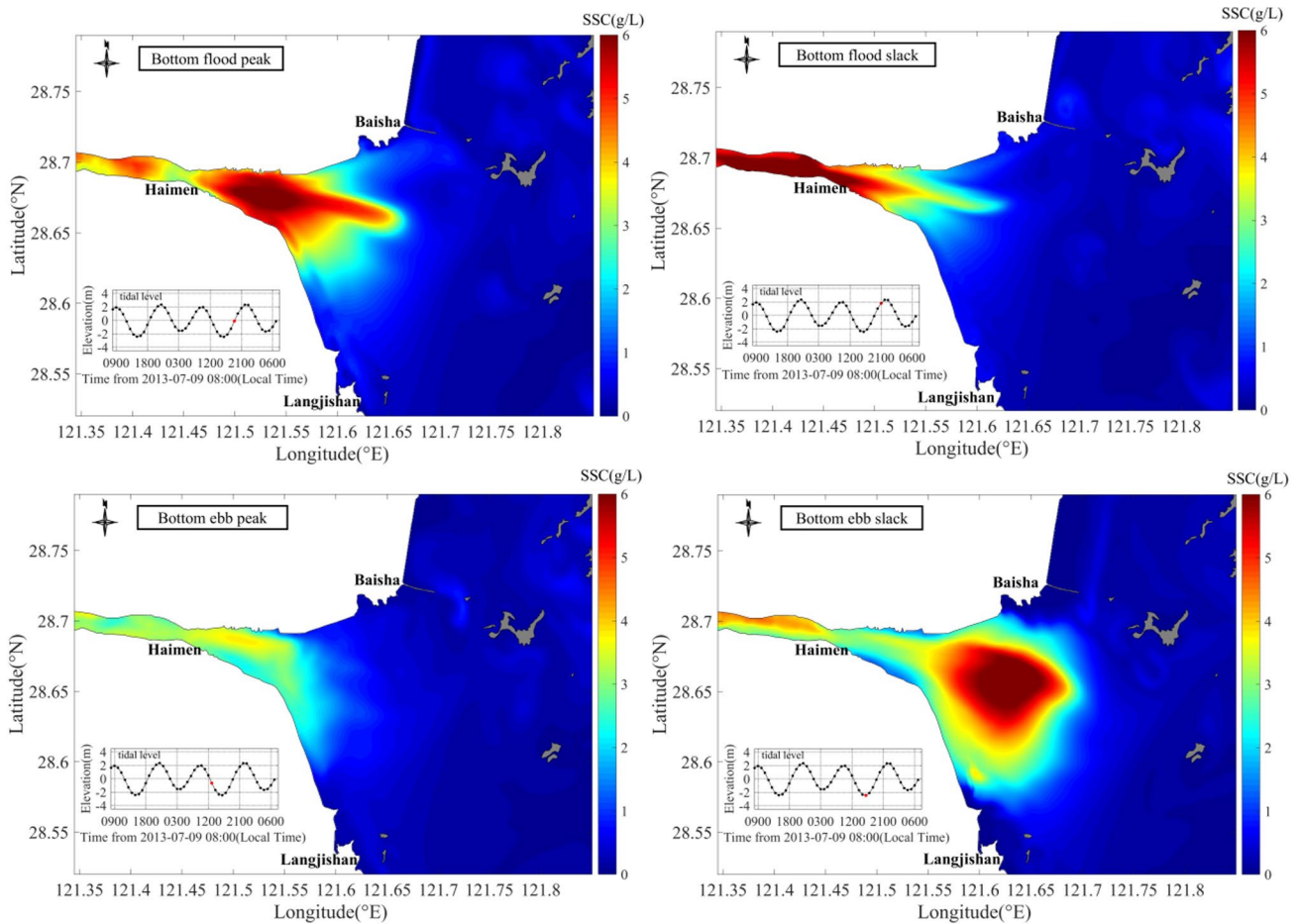
Fig. 7 Distribution of bottom SSC in the Jiaojiang Estuary during the spring tide

than during the spring tides. The mud was mainly located near the main tidal channel near Haimen. The maximum thickness of the fluid mud was approximately 1.2 m. The hydrodynamic force is weak during the neap tides, and the upper water column experiences little erosion from fluid mud. The fluid mud was thicker in the main tidal channel than in the shoals. According to the velocity of fluid mud (Fig. 9), the changes in the distribution of fluid mud thickness are caused by the influence of water depth and

topography (shallow in the shoals and deep in the channel). Fluid mud in the shoal flowed into the main tidal channel.

Fluid mud moves along the main tidal channel of the estuary (Fig. 9). This is because the thickness of the fluid mud varies at different locations, and is affected by water depth, topography, and gravity. Because of the weak entrainment and strong erosion, the thickness of the aggregation center (near Haimen) reaches its maximum
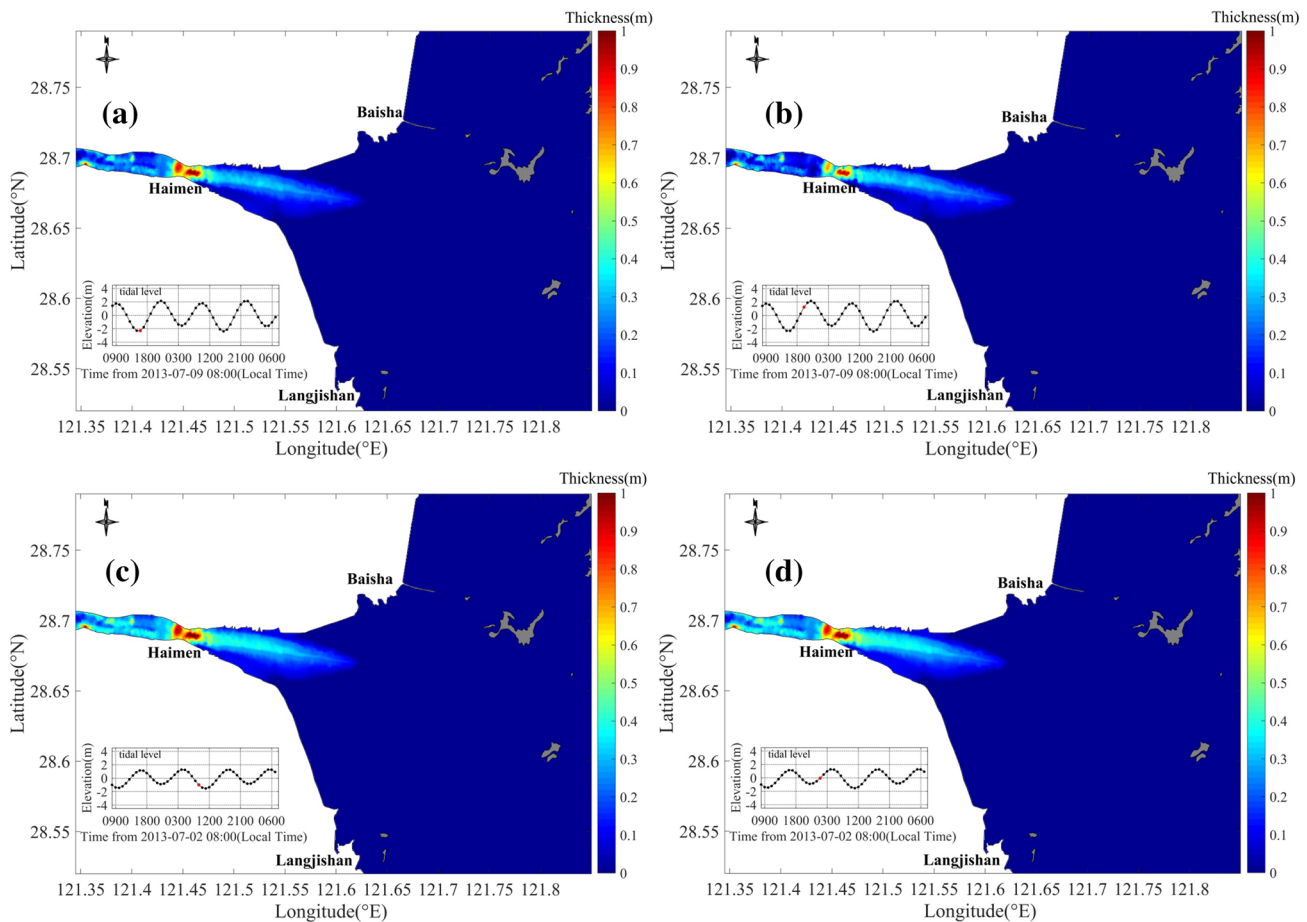
Fig. 8 Thickness of fluid mud during the **a**, **b** spring and **c**, **d** neap tidal periods. The figure shows the moment with the **a**, **c** maximum and **b**, **d** minimum fluid mud areas

value in the deepest area. However, the fluid mud thinned out because of the flow and consolidation of fluid mud and the scouring effect of the upper water.

4.2 Interaction of Water–Fluid Mud–Sea Bed

According to the model results, fluid mud developed along the main tidal channel of the Jiaojiang Estuary. Areas where the fluid mud was the highest and thickest were distributed at Haimen, while there was almost no fluid mud development in the other areas. The deposition process presented a spatially smooth distribution around the area without fluid mud (Fig. 10a). In the absence of fluid mud, the entrainment amount is equal to the erosion amount (Fig. 10b and d). The results indicate a relatively strong flow velocity in the main channel between stations S4 (Haimen) and S6. Hence, at the interface of the fluid mud and upper water, shear stress has a significant scouring effect around S4 and near the main tidal channel (Fig. 10d). Difference between entrainment and

erosion was observed only around the area covered by fluid mud, mainly in the channel between S4 (Haimen) and S6 (Fig. 10b and d). Entrainment is related to the value of U-Um (Eq. 16). The velocity difference between the upper water and fluid mud indicates strong turbulent mixing and active mass exchange at the upper water-fluid mud interface. On the other hand, the velocity of fluid mud was slow (< 0.3 m/s), which is insufficient to generate bottom erosion in the channel covered by fluid mud (Fig. 10d). Consolidation between the fluid mud and the bottom bed occurred only in the high thickness areas of the fluid mud (Fig. 10c). The sink term (sediments leaving the fluid mud layer) is the main effect out of the river mouth, and the sediments are mainly involved in the upper water column, which does not contribute to the formation of fluid mud (Fig. 10e). The domain from Haimen to Niutoujing is mainly controlled by the source term (sediment enters the fluid mud layer) and suspended sediment settlement. The Nanyang and Taizhou shoals on both sides of the estuary
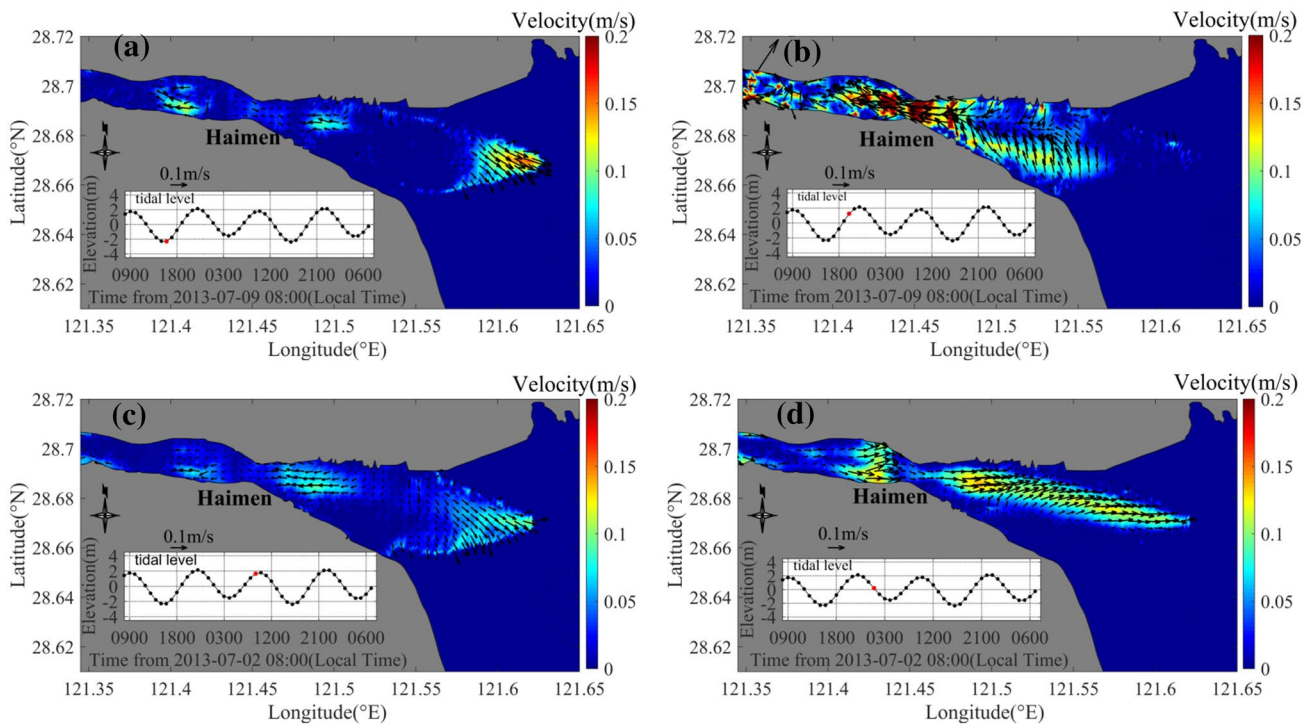
Fig. 9 Velocity of fluid mud during the **a**, **b** spring and **c**, **d** neap tidal periods. The figure shows the moment with the **a**, **c** maximum and **b**, **d** minimum fluid mud areas

also positively contribute to the formation of fluid mud (Fig. 10e).

The distribution of the source-sink term of fluid mud differed between the minimum (Fig. 10e) and maximum (Fig. 10e') moments during neap tides. The minimum distribution moment was comparatively similar to the deposition flux during the maximum moment (Fig. 10a and a'). The tidal currents are weak at the moment of the maximum area of fluid mud, which subsequently weakens the erosion and entrainment processes. The consolidation process of fluid mud is only related to the rate of consolidation and concentration of fluid mud (Formula 18). As these two properties were constant parameters in the model, they inevitably produce uniform consolidation at the interface between the fluid mud and bottom bed (Fig. 10c and c'). The sum of the four source-sink terms of fluid mud indicates that the net contribution from the mud-covered area was positive at the moment of the maximum area during the neap tidal period. (Fig. 10e'). The results indicate that dewatering and entrainment are the main processes involved in the reduction of fluid mud areas.

During spring tides, the distribution of the fluid mud source-sink terms was similar to that during neap tides, but with smaller magnitudes and areas.

4.3 Impact of Suspended Sediments on Residual Currents

To study the influence of high SSC values on hydrodynamics in the Jiaojiang Estuary, residual flow was considered as an example because it is directly related to net sediment transport. Numerical experiments were conducted to investigate the distribution characteristics of the residual flow under the influence of SSC. Case 1 considered the effects of tides, suspended sediments, and fluid mud as the control. Case 2 did not consider the influence of fluid mud, reflecting the impact on fluid mud. Case 3 only considered the tides, reflecting the influence of suspended sediments on the residual flow. The model was run for June and July of 2013. Because fluid mud was mainly near the bottom, we considered the effect of fluid mud on viscosity near the seabed. We referred to the paper by Zhou et al. (2008), and the effect of SSC on the von Karman constant was considered in this model.

The vertical-averaged residual currents accumulated over one month were calculated using the model results. By subtracting the residual currents in Case 1 from those in Case 2, the difference in residual currents was obtained, which indicated the influence of fluid mud (Fig. 11). As illustrated in Fig. 11a, the residual currents caused by fluid mud in Jiaojiang Estuary are small (< 0.09 m/s). The direction of the residual currents in the north of Baishashan is
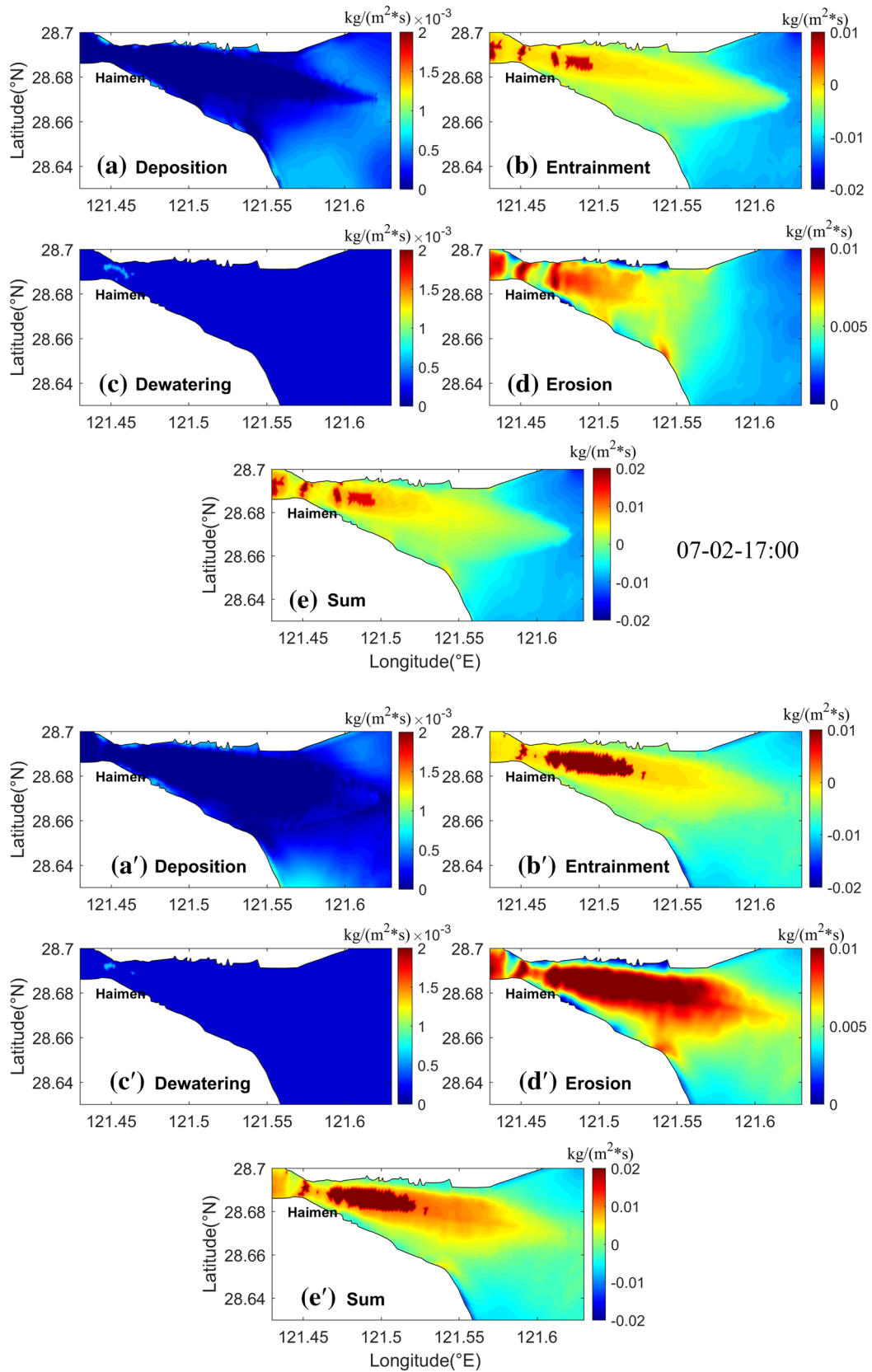
Fig. 10 Distribution of (**a**, **a'**) Deposition (Settling), (**b**, **b'**) Entrainment, (**c**, **c'**) Dewatering, (**d**, **d'**) Erosion, and (**e**, **e'**) Sum of four items in source-sink term. The figure shows the moment with the (**a**–**e**) minimum (**a'**–**e'**) maximum fluid mud areas during neap tides
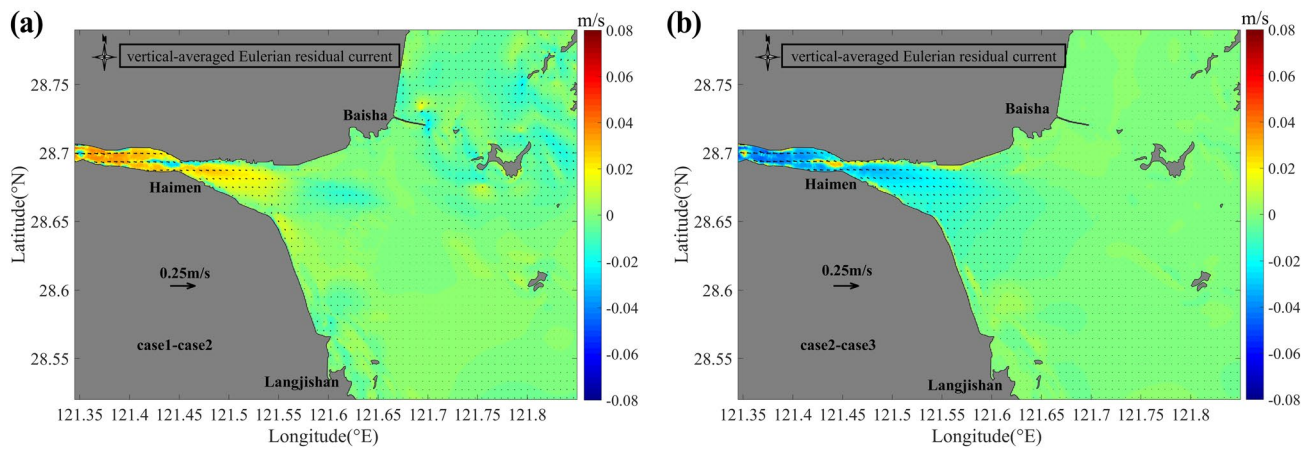
Fig. 11 Distribution of monthly average vertical-averaged Eulerian residual currents: **a** case 1–case 2, **b** case 2–case 3

Table 6 Monthly average vertical-averaged residual currents in numerical tests (cm/s)

Case	B4	B1	B3
1	2.2	6.6	1.8
2	2.1	6.8	1.4
3	4.5	8.5	2.3

Fig. 12 Vertical distribution of $\log10(Ri/0.25)$ along the main tidal channel during spring tides. $\log10(Ri/0.25) > 0$ indicates stratification, $\log10(Ri/0.25) < 0$ indicates mixing

indicating that the residual currents at these stations were affected by fluid mud.

By subtracting the results of Case 2 from those of Case 3, we obtained the difference in the vertical-averaged monthly residual currents, which indicated the influence of SSC (Fig. 11b). The residual currents caused by SSC were small (< 0.08 m/s); the downstream flow was weaker near the southern bank along the coastline, while the northern bank had a strong upstream flow. The overall direction of the flow was into the main tidal channel. Owing to the influence of SSC, the residual currents were weakened. The vertical-integrated residual currents (monthly averaged, comparison of Cases 2 and 3) at B4, B3, and B1 in case 3 increased by 114, 25.0, and 623%, respectively, indicating the great effect of SSC.

4.4 Impacts of Suspended Sediments on Water Stratification

Stratification is an important process in the formation of fluid mud and estuarine turbidity zones. The Richardson number in the tidal period along the main tidal channel of the estuary exhibited clear temporal and spatial variations (Fig. 12). During peak flood (Fig. 12a), the $\log_{10}(Ri/0.25)$ value fluctuates between Haimen and Laoshushan and 20 km from section BL. The maximum value of $\log_{10}(Ri/0.25)$ reached 1.2. The $\log10(Ri/0.25)$ values along the main tidal channel were small, indicating that the water column was less stratified during peak spring flood tides. The Ri value changed from Haimen to section BL during flood slack (Fig. 12b), indicating that the seaward suspended sediments from Haimen causes stratification of the water column. The $\log10(Ri/0.25)$ values between Haimen and Laoshushan increased significantly at the ebb peak (Fig. 12c), with a maximum value of 2.0, indicating that the stratification increased because of the high-SSC. During ebb slack (Fig. 12d), the flow velocity

in the north–south direction. The residual currents near the southern bank are upstream along the coastline, whereas those near the northern bank are downstream. The residual current is largely directed toward the main tidal channel. Therefore, the residual currents weakened owing to the influence of the fluid mud. The vertical-averaged residual currents accumulated in one month (Table 6, comparison between Case 1 and Case 2) at stations B4, B3, and B1 in Case 2 decrease by 4.5, − 3.1, and 22.2%, respectively,

Fig. 13 Horizontal distribution of potential energy anomalies in the Jiaojiang Estuary during spring tides
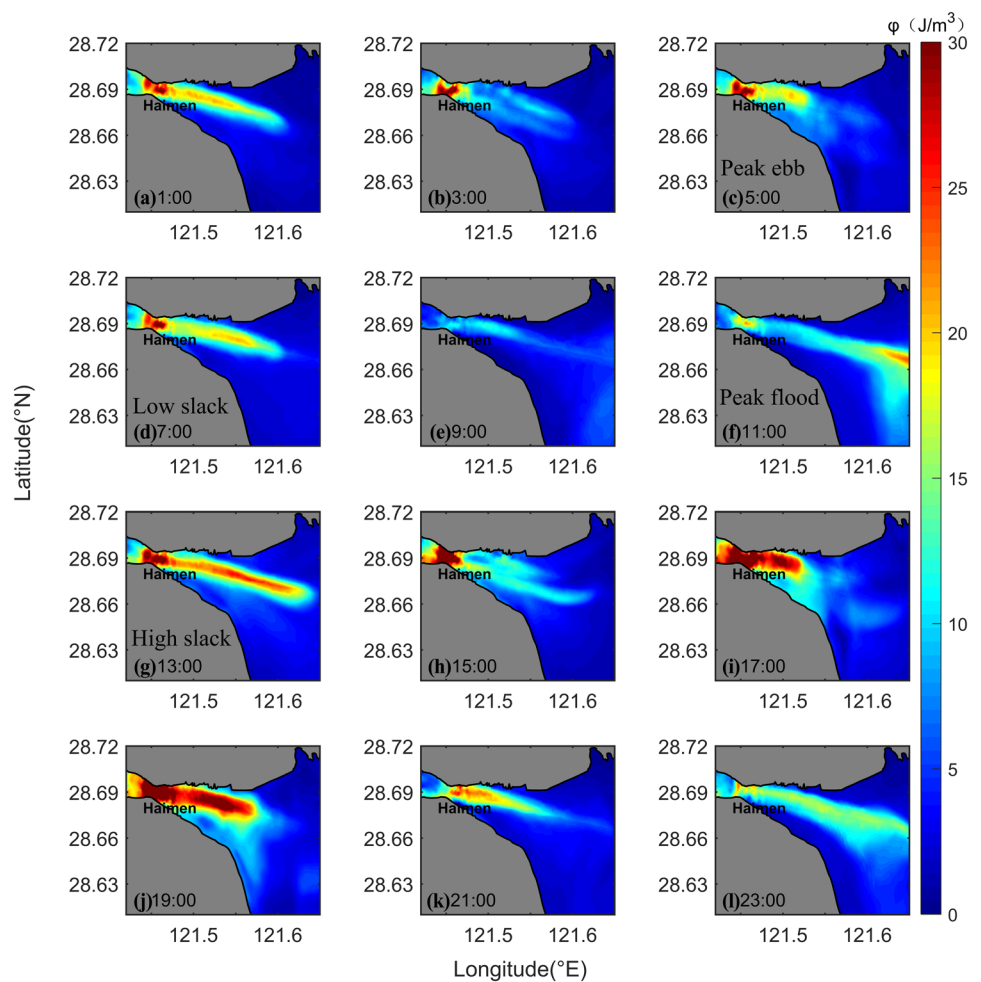
was weaker, with decreased SSC; therefore, the stratification intensity weakened compared with that at the time of the ebb slack.

The *Ri* value of the ebb tides was larger than that of the flood tide, which is the effect of shear asymmetry on the SSC distribution. The landward tidal currents partly offset the seaward runoff during the spring tide period, which was superimposed with a strong circulation, resulting in a weak shear during the flood tide, further reducing the vertical SSC gradient. In contrast, the vertical SSC gradient in the water column increased during the ebb tide. This shear asymmetry dominates the stratification changes.

Compared with the spring tide period, the stratification increased between Haimen and Laoshushan and was distributed more widely during the neap tidal period. Stratification of the water column increased along the main tidal channel at the ebb slack, with widening distribution.

The distribution of potential energy anomalies in the Jiaojiang Estuary during the spring tide is presented in Fig. 13. The interval between each figure part is 2 h. During peak flood tides (Fig. 13f), the φ was small and fluctuated along the main tidal channel, indicating a less stratified water column. φ increases at the high slack (Fig. 13g), indicating that the seaward SSC from Haimen resulted in partial stratification of the water column. During the ebb tides, the maximum value of the potential energy anomaly φ near Haimen was greater than 30 J/m^3 (Fig. 13c), and high turbidity enhanced the stratification. The maximum values of φ at peak flood (Fig. 13f), high slack (Fig. 13g), and low slack (Fig. 13d) were 18, 28, and 27 J/m^3, respectively. Stratification caused by sediments in the spring tidal period was strong and lasted for a long time (> 50% of the tidal period).

Horizontal distribution of the potential energy difference reflects the spatial variation in the water stratification. The variation of φ along the main tidal channel was large in the spring tidal period; for example, the change in φ was more than 25 J/m^3 at high slack (Fig. 13g). The variation in φ in the lateral section of the estuary was approximately 5–20 J/m^3. The spatial and temporal variation in φ during the neap tide period was weaker, and the distribution trend was similar to that during the spring tide.

5 Conclusions

Combining field data on tides and sediments and a well-calibrated sediment numerical model of the Jiaojiang Estuary, we analyzed the characteristics of suspended sediment dynamics and their correlation with hydrodynamics in the estuary. The main conclusions are as follows.

(1) SSC and sediment transport rate are closely related to the flow velocity in the low-frequency region during both spring and neap tides. The tidal variation in flow velocity and water level leads to a fluctuation in SSC during a tidal cycle and is the key to the fluctuation in the sediment transport rate.

(2) Tidal currents, SSC, and fluid mud change spatially and temporally in a tidal cycle. The flow velocity and SSC were higher during spring tides than during neap tides. The flow is flood-dominated and causes a higher SSC during a flood than during an ebb. Fluid mud is formed in the main tidal channel and varies with tides, with larger areas observed during neap tides. The velocity of the fluid mud was less than 0.3 m/s. The sink and source processes control the fluid mud dynamics.

(3) Sediments weaken the seaward residual currents and amplify the stratification by changing the water viscosity and density, respectively. Numerical results revealed that the sediments and fluid mud slightly weakened the seaward residual currents. Owing to the sediments, stratification was stronger during spring tides than neap tides, and weaker during flood tides than ebb tides. The stratification was stronger along the main tidal channel than in the shoal.

References

Allen JI, Somerfield PJ, Gilbert FJ (2007) Quantifying uncertainty in high–resolution coupled hydrodynamic–ecosystem models. J Marine Syst 64(1–4):3–14. https://doi.org/10.1016/j.jmarsys.2006.02.010

Bi AH, Sun ZL (1984) Preliminary study on the process of Jiaojiang estuary. J Sediment Res 3:14–28. https://doi.org/10.16239/j.cnki.0468-155x.1984.03.002(inChinese)

Bigg PH (2002) Density of water in SI units over the range 0–40°C. Brit J Appl Phys 18(4):521–525. https://doi.org/10.1088/0508-3443/18/4/315

Blake AC, Kineke GC, Milligan TG, Alexander CR (2001) Sediment trapping and transport in the ACE Basin. South Carolina Estuaries 24(5):721–733

Burchard H, Hetland RD, Schulz E, Schuttelaars HM (2011) Drivers of residual estuarine circulation in tidally energetic estuaries: straight and irrotational channels with parabolic cross section. J Phys Oceanogr 41(3):548–570. https://doi.org/10.1175/2010JPO4453.1

Cao ZD, Xiao H (2010) Using hydrological data to predict the evolution trend of seabed erosion and deposition. Port Waterw Eng 2:20–22 (in Chinese). https://doi.org/10.16233/j.cnki.issn1002-4972.2010.02.014

Chen C, Liu H, Beardsley RC (2003) An unstructured grid, finite–volume, three–dimensional, primitive equations ocean model: application to coastal ocean and estuaries. J Atmos Ocean Tech 20(1):159–186. https://doi.org/10.1175/1520-0426(2003)020%3c0159:AUGFVT%3e2.0.CO;2

Corbett DR, Dail M, Mckee B (2007) High–frequency time–series of the dynamic sedimentation processes on the western shelf of the Mississippi River Delta. Cont Shelf Res 26(10–11):1600–1615. https://doi.org/10.1016/j.csr.2007.01.025

Dankers PJT, Winterwerp JC (2007) Hindered settling of mud flocs: theory and validation. Cont Shelf Res 27(14):1893–1907. https://doi.org/10.1016/j.csr.2007.03.005

Dong LX (1998) Classification of highly turbid Jiaojiang Estuary. Acta Oceanol Sin 4:469–482

Dong LX, Wolanski E, Li Y (1997) Field and modeling studies of fine sediment dynamics in the extremely turbid Jiaojiang River estuary. China J Coastal Res 13(4):995–1003

Dyer KR (1986) Coastal and estuarine sediment dynamics. John Wiley & Sons, Chichester, p 358. https://doi.org/10.1002/9781118669280.oth1

Einstein HA, Chien N (1955) Effects of heavy sediment concentration near the bed on velocity and sediment distribution. Omaha, Missouri River Division, Corps of Engineers, US Army, p 78

Fu NP, Bi AH (1989) Discussion on some problems of suspended sediment movement in Jiaojiang. J Sediment Res 3:51–57 (in Chinese). https://doi.org/10.16239/j.cnki.0468-155x.1989.03.007

Geyer WR (1993) The importance of suppression of turbulence by stratification on the estuarine turbidity maximum. Estuaries 16(1):113–125

Geyer WR, Maccready P (2014) The estuarine circulation. Annu Rev Fluid Mech 46(1):175–197. https://doi.org/10.1146/annurev-fluid-010313-141302

Guan WB, Kot SC, Wolanski E (2005) 3–D fluid–mud dynamics in the Jiaojiang Estuary. China Estuar Coast Shelf S 65(4):747–762. https://doi.org/10.1016/j.ecss.2005.05.017

He J, Chu J, Tan SK, Vu TT, Lam KP (2017) Sedimentation behavior of flocculant–treated soil slurry. Mar Georesour Geotec 35:593–602. https://doi.org/10.1080/1064119X.2016.1177625

Holzman B (1943) The influence of stability on evaporation. Ann NY Acad Sci 44(1):13–18. https://doi.org/10.1111/j.1749-6632.1943.tb31289.x

Jeuken MCJL, Wang ZB (2010) Impact of dredging and dumping on the stability of ebb–flood channel systems. Coast Eng 57(6):553–566. https://doi.org/10.1016/j.coastaleng.2009.12.004

Jiang J, Wolanski E (1998) Vertical mixing by internal wave breaking at the lutocline, Jiaojiang River estuary. China J Coastal Res 14(4):1426–1431

Jiang CX (2017) Numerical simulation research on the sediment settling characteristics in the strong tidal current estuarine environment–Take Jiaojiang Estuary of Zhejiang coastal area as an example. M.Sc. Thesis, Zhejiang University, p 94 (in Chinese)

Kerner M (2007) Effect of deepening the Elbe Estuary on sediment regime and water quality. Estuar Coast Shelf S 75(4):492–500. https://doi.org/10.1016/j.ecss.2007.05.033

Li Y, Wolanski E, Xie Q (1993) Coagulation and settling of Suspended sediment in the Jiaojiang River estuary. China J Coastal Res 9(2):390–402

Liu XS, Lu JY, Liao XY, Wu CH (2014) Research status and existing problems of Carmen constant. J Yangtze River Sci Res Inst 31(6):1–6 (in Chinese). https://doi.org/10.3969/j.issn.1001-5485.2014.06.001

Liu W, Fan DD, Tu JB, Lu J (2018) Suspended transportation and flux mechanism of sediment in the Jiaojiang Estuary in spring. Mar Geol Quat Geol 38(1):41–51 (in Chinese). https://doi.org/10.16562/j.cnki.0256-1492.2018.01.005

Liu JB, Ma RB, Yuan YD, Yang XM, Ma WM (2021) Linear stability of a fluid mud–water interface under surface linear long travelling wave based on the Floquet theory. Eur J Mech B-Fluids 86:37–48. https://doi.org/10.1016/j.euromechflu.2020.11.008

Mcanally WH, Friedrichs C, Hamilton D, Hayter E (2007) Management of fluid mud in estuaries, bays, and lakes. I: present state of understanding on character and behavior. J Hydraul Eng 133(1):9–22. https://doi.org/10.1061/(ASCE)0733-9429(2007)133:1(9)

Mellor GL, Yamada T (1982) Development of a turbulent closure model for geophysical fluid problems. Rev Geophys 4(20):851–875. https://doi.org/10.1029/RG020i004p00851

Monge-Ganuzas M, Cearreta A, Evans G (2013) Morphodynamic consequences of dredging and dumping activities along the lower Oka estuary (Urdaibai Biosphere Reserve, southeastern Bay of Biscay, Spain). Ocean Coast Manage 77:40–49. https://doi.org/10.1016/j.ocecoaman.2012.02.006

Ni JR, Hui YJ (1988) Relationship between velocity distribution of muddy water and suspended matter concentration distribution. J Sediment Res 2:19–30 (in Chinese). https://doi.org/10.16239/j.cnki.0468-155x.1988.02.003

Pu X, Shi JZ, Hu GD, Xiong LB (2015) Circulation and mixing along the North Passage in the Changjiang River Estuary, China. J Marine Syst 148:213–235. https://doi.org/10.1016/j.jmarsys.2015.03.009

Qin RY (1991) Study on the variation of Carmen constant of moving bed flow. J Sediment Res 3:38–52 (in Chinese). https://doi.org/10.16239/j.cnki.0468-155x.1991.03.007

Shi JZ, Gu WJ, Wang DZ (2008) Wind wave–forced fine sediment erosion during the slack water periods in Hangzhou bay, China. Environ Geol 55:629–638. https://doi.org/10.1007/s00254-007-1013-2

Shu AP, Fei XJ (2008) Sediment carrying capacity of high sediment–laden flow. Scientia Sinica G 6:653–667 (in Chinese)

Smagorinsky J (1963) General circulation experiments with the primitive equations. Mon Weather Rev 3(91):99–164. https://doi.org/10.1175/1520-0493(1963)0912.3.CO;2

Tran D, Strom K (2019) Floc sizes and resuspension rates from fresh deposits: influences of suspended sediment concentration, turbulence, and deposition time. Estuar Coast Shelf S 229:106397. https://doi.org/10.1016/j.ecss.2019.106397

Uncles RJ, Bloomer NJ (2000) Seasonal variability of salinity, temperature, turbidity and suspended chlorophyll in the Tweed Estuary. Sci Total Environ 251–252:115–124. https://doi.org/10.1016/S0048-9697(00)00405-8

Van Maren DS, Van Kessel T, Cronin K, Sittoni L (2015) The impact of channel deepening and dredging on estuarine sediment concentration. Cont Shelf Res 95:1–14. https://doi.org/10.1016/j.csr.2014.12.010

Wan YY, Dano R, Li WH, Qi DM, Gu FF (2014) Observation and modeling of the storm–induced fluid mud dynamics in a muddy–estuarine navigational channel. Geomorphology 217:23–36. https://doi.org/10.1016/j.geomorph.2014.03.050

Wang SY (1981) Variation of Carmen constant in sediment–laden flow. J Hydr Div–ASCE 107(11):407–417. https://doi.org/10.1061/JYCEAJ.0005645

Wang XH (2002) Tide–induced sediment resuspension and the bottom boundary layer in an idealized estuary with a muddy bed. J Phys Oceanogr 32(11):3113–3131. https://doi.org/10.1175/1520-0485(2002)0322.0.CO;2

Wang ZY, Nestmann F, Larsen P, Dittrich A (1998) Resistance and drag reduction of flows of clay suspensions. J Hydraul Eng 124(1):41–49. https://doi.org/10.1061/(ASCE)0733-9429(1998)124:1(41)

Wang GY (2007) A 2D numerical simulation of suspended sediment in the Taizhou Bay. M.Sc. Thesis, Zhejiang University, p 61 (in Chinese)

Winterwerp JC, Van Kesteren WGM (2006) Introduction to the physics of cohesive sediment in the marine environment. Cambridge University Press

Winterwerp JC, Wang ZB (2013) Man–induced regime shifts in small estuaries–I: theory. Ocean Dynam 63(11):1279–1292. https://doi.org/10.1007/s10236-013-0662-9

Wright LD (1989) Benthic boundary layers of estuarine and coastal environments. Rev Aquat Sci 1:75–95

Xia YZ (2014) The attenuation of shallow–water waves over seabed mud of a stratified viscoelastic model. Coast Eng J 56(4):1450021. https://doi.org/10.1142/S0578563414500211

Xia YZ, Zhu KQ (2011) Fractional–order Maxwell model of seabed mud and its effect on surface–wave damping. Appl Math Mech-Engl 32(11):1357–1366. https://doi.org/10.1007/s10483-011-1506-x

Xie QC, Li BG, Xia XM, Li Y (1998) Vertical distributions of suspended matter and lutoclines in the Jiaojiang Estuary. Acta Oceanol Sin 20(6):58–69 (in Chinese)

Xie M, Wei Z, Guo W (2010) A validation concept for cohesive sediment transport model and application on Lianyungang Harbor. China Coast Eng 57(6):585–596. https://doi.org/10.1016/j.coastaleng.2010.01.003

Xie D, Pan C, Gao S, Wang ZB (2018) Morphodynamics of the Qiantang Estuary, China: controls of river flood events and tidal bores. Mar Geol 406:27–33. https://doi.org/10.1016/j.margeo.2018.09.003

Xu XS, Zhang XZ, Li Q, Xia WY, Zhao XD (2018) Water and sediment characteristics and maximum turbidity simulation of Jiaojiang River. Port Waterw Eng 12:143–151 (in Chinese). https://doi.org/10.16233/j.cnki.issn1002-4972.20181130.004

Xu CY, Chen YP, Pan Y, Yu LL (2020) The effects of flocculation on the entrainment of fluid mud layer. Estuar Coast Shelf S 240:106784. https://doi.org/10.1016/j.ecss.2020.106784

Yang XC, Zhang QH, Hao LN (2015) Numerical investigation of fluid mud motion using a three–dimensional hydrodynamic and two–dimensional fluid mud coupling model. Ocean Dynam 65(3):449–461. https://doi.org/10.1007/s10236-015-0815-0

Yang XC (2014) Numerical simulation of fluid mud formation and movement on muddy coast. M.Sc. Thesis, Tianjin University, p 150 (in Chinese)

Zhang HW (1995) The formula of vertical distribution of sediment–laden flow velocity. J Sediment Res 2:1–10 (in Chinese). https://doi.org/10.16239/j.cnki.0468-155x.1995.02.001

Zhao LB (1992) The effect of salt–freshwater mixing in Jiaojiang Estuary. Mar Sci 1:61–64 (in Chinese)

Zhao GB, Bian CW, Xu JP (2019) A field study of shear stress and suspended sediment concentration in the bottom boundary layer under the influences of tidal currents and wind waves. Period Ocean Univ China 49(11):83–91 (in Chinese). https://doi.org/10.16441/j.cnki.hdxb.20180413

Zheng YQ (2021) Study on hydrodynamics and sediment transport characteristics in the Jiaojiang Estuary. M.Sc. Thesis, Zhejiang University, p 126 (in Chinese)

Zhou YL, Tang HW, Yan J, Xu ZG, Guo Q (2008) The influencing factors of Carmen constant of sediment carrying flow. J Sediment Res 3:51–56 (in Chinese). https://doi.org/10.16239/j.cnki.0468-155x.2008.03.007